Supporting Information for

Aggregation Structure of Chiral Cubic Liquid Crystals

Revealed by X-ray Diffraction Utilizing a New Algorithm

Toshihiko Oka,[†] Yasuhisa Yamamura,[‡] Shoichi Kutsumizu,[¶] and Kazuya Saito*,[‡]

[†]*Department of Physics, Faculty of Science, and Nanomaterials Research Division, Research Institute of Electronics, Shizuoka University, Shizuoka 422-8529, JAPAN*
[‡]*Department of Chemistry, Faculty of Pure and Applied Sciences, University of Tsukuba, Tsukuba, Ibaraki 305-8571, JAPAN*
[¶]*Department of Chemistry and Biomolecular Science, Faculty of Engineering, Gifu University, Yanagido, Gifu 501-1193, JAPAN*

- Definition of indicators

- Extension of the phase retrieval method for powder diffractions

- Input data for analyses
    Figure S1. Uncorrected diffraction patterns of BABH(14) and BABH(15)
    Table S1. Observed X-ray diffraction intensities

- Summary of analyses

    Figure S2. Summary of the analysis for BABH(14)
    Figure S3. Summary of the analysis for BABH(15)
    Figure S4. Electron density distribution of BABH(15)
    Figure S5. Close-up of electron density distribution of BABH(14)
                showing a distorted six-membered circuit
    Figure S6. Comparison of experimentally deduced and ideal *noh* nets
    Figure S7. Illustration of the chiral cubic and achiral (Gyroid) phases in terms of triangles
    Table S2. Phase sequence and some geometric quantities of BABH(14) and BABH(15)

- Discussion reaching to the aggregation model.

<u>Definition of indicators</u>

We have two indicators of electron density quality to be minimized in the employed algorithm.

The first senses the flatness of the electron density distribution $\rho(\boldsymbol{r})$ as a function of position $\boldsymbol{r} = (x, y, z)$ defined as

$$I_\rho = \max\{\rho(\boldsymbol{r})\} - \min\{\rho(\boldsymbol{r})\}.$$

The second reflects the implausibility of isolated maximum and minimum of $\rho(\boldsymbol{r})$. The index I_K is defined as

$$I_K = \int_C |\det H(\boldsymbol{r})| d\boldsymbol{r},$$

where the integration is taken over the region where $\rho(\boldsymbol{r})$ is strictly convex in a unit cell. The matrix H is a Hessian of $\rho(\boldsymbol{r})$ defined by

$$H = \begin{pmatrix} \rho_{xx} & \rho_{xy} & \rho_{xz} \\ \rho_{yx} & \rho_{yy} & \rho_{yz} \\ \rho_{zx} & \rho_{zy} & \rho_{zz} \end{pmatrix},$$

where subscripts indicate partial derivatives by them.
See refs. s1 and s2 for details of the algorithm.

Extension of the phase retrieval method for powder diffractions

In the powder diffraction data of cubic crystals, diffraction peaks from the planes with the same $|\boldsymbol{h}|^2$ ($= h^2 + k^2 + l^2$) overlap perfectly. The observed peak intensity after appropriate corrections can be written as follows:

$$I_{\mathrm{obs}}(|\boldsymbol{h}|^2) = \sum_{i=1}^{n} \left[\sum_{\boldsymbol{h}_i \in H_i} |F(\boldsymbol{h}_i)|^2 \right],$$

where, $|\boldsymbol{h}|^2 = |\boldsymbol{h}_i|^2$, $F(\boldsymbol{h})$ is a structure factor, H_i is a set of indices with equivalent structure factor amplitudes, and n is the number of the sets. For example, for the Laue class $m\bar{3}$, $|\boldsymbol{h}|^2 = 10$ yields $n = 2$, $H_1 = \{310\}$, and $H_2 = \{130\}$ (see Table S1). $|F(\boldsymbol{h}_i)|$ is the same as long as $\boldsymbol{h}_i \in H_i$. The basic algorithm of the phase retrieval is almost the same as ref. s2. Since the previous algorithm is for single crystal diffraction data, we modified it for powder data. Suppose that the structure factor $G(\boldsymbol{h})$ is obtained in step 3 of the previous algorithm. For powder diffraction data, the equation for the new structure factor in step 4 is modified as follows:

$$F(\boldsymbol{h}_1) = \begin{cases} \left[\left(\dfrac{I_{\mathrm{obs}}(|\boldsymbol{h}|^2)}{\sum_{\boldsymbol{h}_1 \in H_1} \overline{|G(\boldsymbol{h}_1)|}^2 + \sum_{\boldsymbol{h}_2 \in H_2} \overline{|G(\boldsymbol{h}_2)|}^2} \right)^{\frac{1}{2}} \overline{|G(\boldsymbol{h}_1)|} \right] \left\{ \dfrac{G(\boldsymbol{h}_1)}{|G(\boldsymbol{h}_1)|} \right\} & \boldsymbol{h}_1 \in H_{\mathrm{obs}} \\ 0 & \boldsymbol{h}_1 \notin H_{\mathrm{obs}} \end{cases}$$

where

$$\overline{|G(\boldsymbol{h}_1)|} = \sum_{\boldsymbol{h}_1 \in H_1} |G(\boldsymbol{h}_1)| \Big/ \sum_{\boldsymbol{h}_1 \in H_1} 1 ,$$

and H_{obs} is the set of all $\boldsymbol{h}$ combinations for which the structure factor was observed. The [] and {} parts in the equation correspond to the amplitude and phase parts of the structure factor, respectively. This constraint is also applied after the initial generation of the random structure factors. Other than this, the algorithm is the same as in the previous paper.
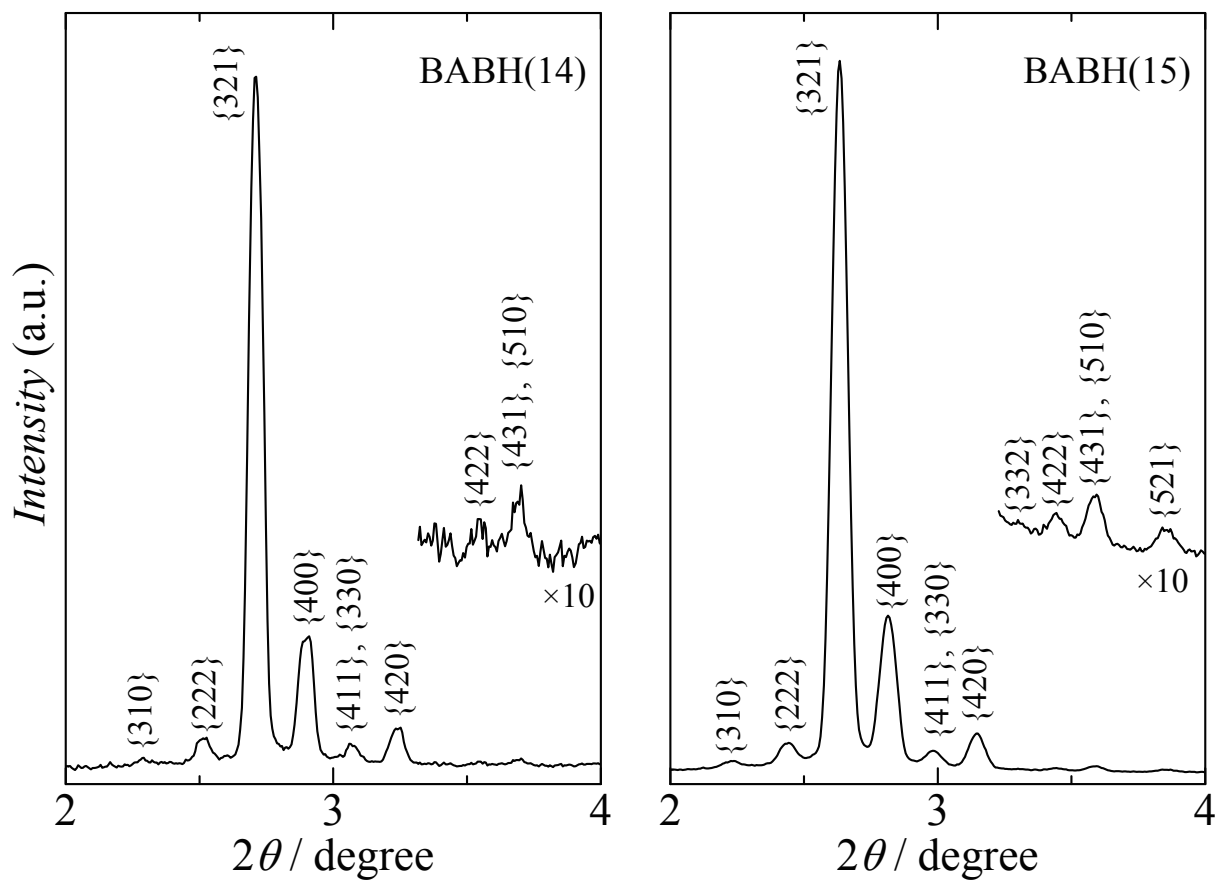
Input data for analyses

Figure S1. Diffraction patterns of BABH(14) (424.1 K) and BABH(15) (418.3 K), the row data for [s3].

Table S1. Observed X-ray diffraction intensities [s3]. The Laue class is $m\bar{3}$.

$|\boldsymbol{h}|^2$	I_{obs}		n[a]	overlapping $\boldsymbol{h}$ sets (multiplicity)			
	BABH(14)	BABH(15)					
10	0.747	0.698	2	{310} (12)	{130} (12)		
12	1.344	1.290	1	{222} (8)			
14	27.728	25.024	2	{321} (24)	{231} (24)		
16	6.000	6.000	1	{400} (6)			
18	1.231	0.952	2	{411} (24)	{330} (12)		
20	1.638	1.433	2	{420} (12)	{240}(12)		
22	-	0.106	1	{332} (24)			
24	0.350	0.198	1	{422} (24)			
26	0.209	0.217	4	{431} (24)	{341} (24)	{510} (12)	{150} (12)
30	-	0.091	2	{521} (24)	{251} (24)		

[a]The number of overlapping $\boldsymbol{h}$ sets.

4

Summary of analyses

Starting from initial electron density distributions computed with 100 guess sets of random phases of experimental structure factors, the iterative modifications while keeping structure factor norms towards a smaller value of the indicator, I_ρ, under the algorithm converged to densities with locally minimum indicators. In the calculations, the parameters were set to $v_f = 0.35$ (volume fraction of positive electron density region), $k_t = 1.3{\sim}0.8$ (flipping parameter, period 41), $k_t = 1.0{\sim}0.0$ (threshold parameter, period 43), and the number of iterations was 7000. Figures S2a and S3a show the indicator combinations for BABH(14) and BABH(15), respectively. The electron density distributions of 20 and 14 trials encircled by a red circle for each are identical. Others (51 and 65 attempts) at the lower-left corner [$I_\rho < 26$ and 24 for BABH(14) and BABH(15), respectively] are also identical with slight distortion to the best results. The obtained electron densities (and phases of structure factors) were translated to match the conventional origin of the determined space group $I2_13$. The final structure factors are shown in Table 1 of the main text. The lower panels (b and c) of Figs. S1 and S2 indicate the norms of the structure factors and phases calculated from the best electron densities as a function of $h^2 + k^2 + l^2$. The Laue class $m\bar{3}$ allows different norms of (hkl) and (khl) while reserving the identity for their cyclic permutations. The positive/negative symmetry of the phase reflects the Friedel law. Figures S4 and S5 show the electron density distribution of BABH(15) and a close-up of that of BABH(14), respectively. Analyses of the electron density indicated that local maxima well represent the skeletal graphs. Fractional coordinates of the vertices (up to two digits) are (0.17, 0.17, 0.17), (0.34, 0.34, 0.34), (0.65, 0.57, 0.37), and (0.62, 0.34, 0.47). The first and last halves are on a body diagonal and at general positions, respectively. The network geometry is compared with the ideal *noh* net in Fig. S6. Table S2 summarizes some quantities derived from the aggregation model. Figure S7 displays alternative representations of the connectivity (line graph) of the electron density distribution.
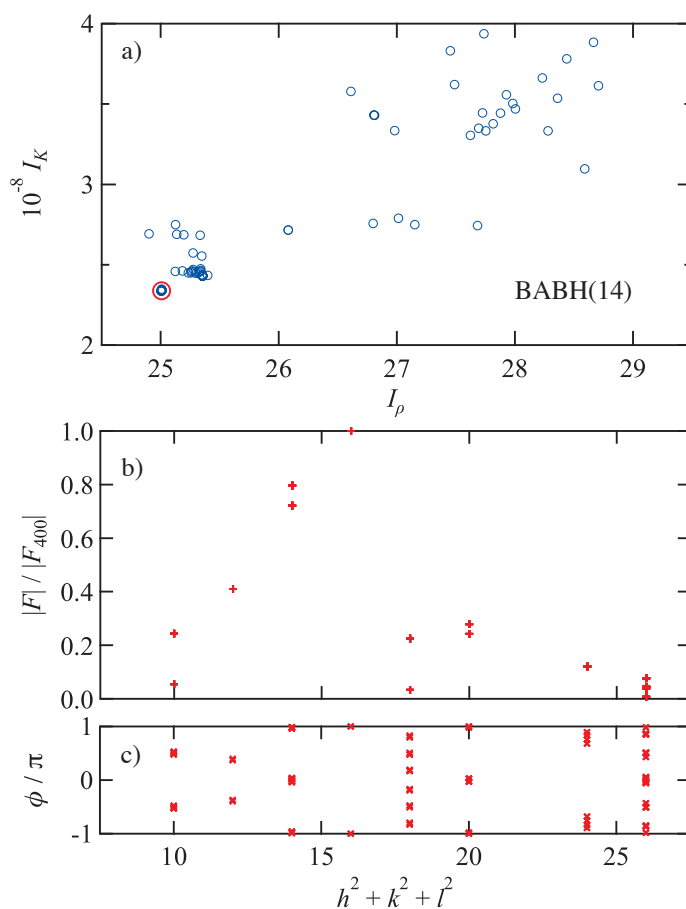

Figure S2. Summary of the analysis for BABH(14). a) Distribution of indicator combinations for BABH(14). The chosen solution is marked by a red circle; b) Distribution of |F|; c) Distribution of the phase divided by π.

Figure S3. Summary of the analysis for BABH(15). a) Distribution of indicator combinations for BABH(15). The chosen solution is marked by a red circle; b) Distribution of $|F|$; c) Distribution of the phase divided by π.
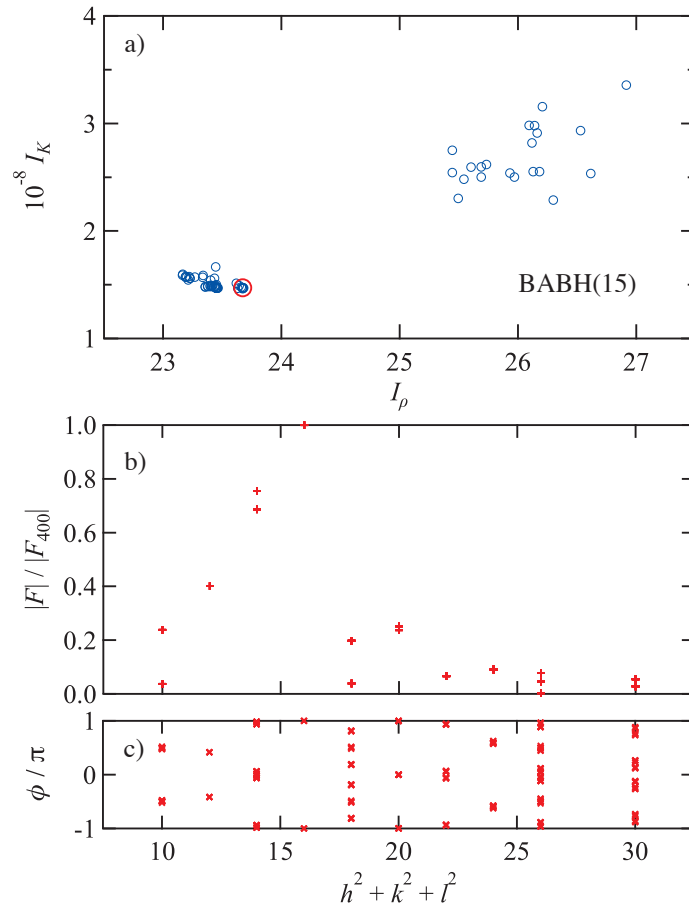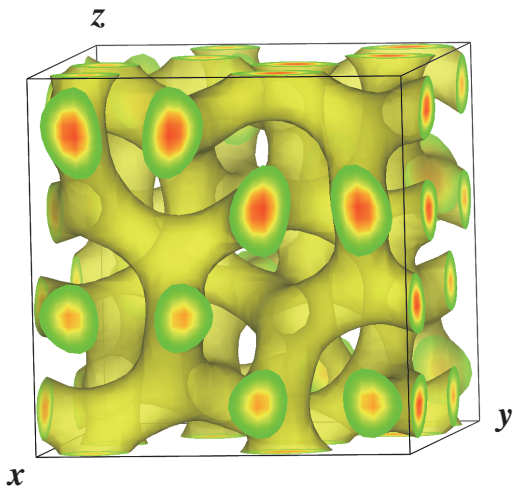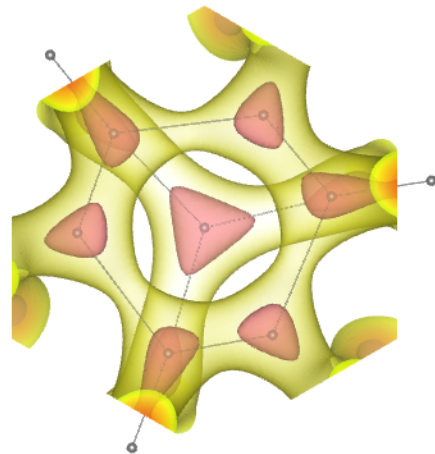

Figure S4. Electron density distribution of BABH(15).

Figure S5. Close-up of electron density distribution of BABH(14) viewed along the [111] (threefold axis). The distortion of the six-membered circuit is evident.
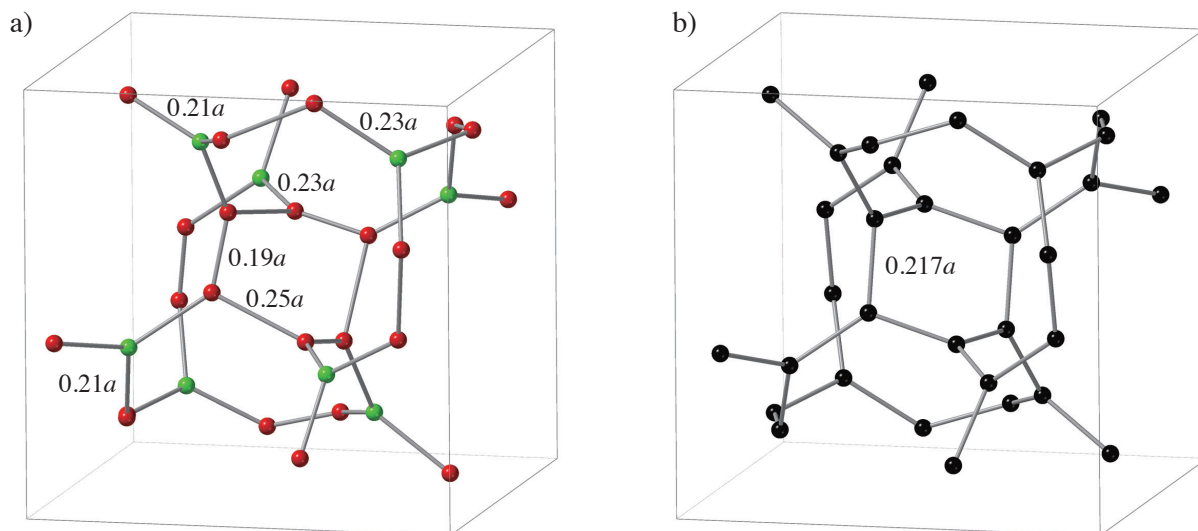
Figure S6. Comparison of the (a) experimentally deduced and (b) ideal *noh* nets. Colors in a) distinguish the vertices on a threefold axis and at a crystallographically general position. Distances between selected vertices are shown in a) in unit of the cell constant, *a*, whereas all distances in the ideal *noh* net (with completely flat junctions) are equal. In reality, there is another net related by a half translation along the body diagonal in (a).

Table S2. Phase sequence against the temperature of BABH(14) and BABH(15) and some quantities derived from the structural analysis for chiral $I2_13$ and achiral $Ia\bar{3}d$/Gyroid phases

Phase sequence

BABH(14): crystal – 402.6 K –> chiral cubic phase – 432.1 K –> isotropic liquid
BABH(15): crystal – 402.6 K –> chiral cubic phase – ca. 430 K –>
$\qquad$ Gyroid ($Ia\bar{3}d$) phase – 432.2 K –> isotropic liquid

	BABH(14)	BABH(15)	
phase	chiral phase	chiral phase	achiral phase
a / nm	12.20 (424.1 K)	12.56 (418.3 K)	7.98 (429.5 K)
number of molecules in a cell[†]	1600	1700	440
space group	$I2_13$ (No. 199)	$I2_13$ (No. 199)	$Ia\bar{3}d$ (No. 230)
number of junctions in a cell	64	64	16
number of molecules per junction	25	27	28
linear distance between bonding junctions[‡]	2.53 nm, 2.81 nm 2.29 nm, 3.08 nm	2.52 nm, 2.98 nm 2.38 nm, 3.17 nm	2.82 nm 2.82 nm
linear distance between non-bonding junctions[⹊]	3.72 nm	3.92 nm	3.46 nm

[†]Assuming the bulk density of 1.00 g cm⁻³.

[‡] For the chiral phase, the upper line contains ones including a vertex on a threefold axis, whereas the lower line ones on the six-membered ring.

  No assumption is necessary for the $Ia\bar{3}d$ phase ($\sqrt{2}a/4$) because of the symmetry.

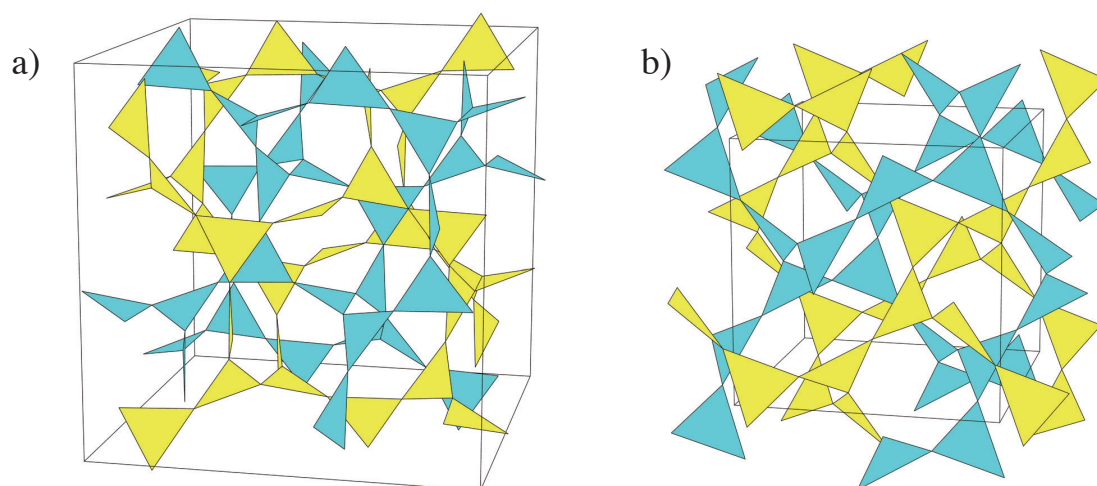[⹊]Distance between nearest junctions on a body diagonal of the cell.

Figure S7. Idealized illustration of structures of a) chiral $I2_13$ and b) achiral $I a\bar{3}d$/Gyroid phases in terms of planar triangles, which are cores of aggregated molecular cores.

Discussion reaching to the aggregation model

Based on the entropic and other evidence of molten states of alkyl chains in most liquid crystals [s4-s6], our thermodynamic [s7] and structural [s8] studies indicated that a fundamental aggregation mode of (layered) smectic liquid crystals of chain-core type mesogenic molecules is the alternating stack of core and chain layers. Further, our experiments [s9,10] and the survey of existing literature [s11] revealed that many orthogonal smectics (smectic A, B, and E phases) exhibit one of two dependencies of their layer spacings, 0.19 nm $(CH_2)^{-1}$ and 0.14 nm $(CH_2)^{-1}$, where the CH_2 means that in an alkyl chain in a molecule. Since both magnitudes are larger than expected for a single highly-disordered alkyl chain, the smectic aggregation must contain layers to which alkyl groups from both sides contribute [s9-s11]. The former dependence is reasonable for the increment of chains normal to the layer on average. The smaller dependence of the latter indicates the inclination of the alkyl chain from the layer normal. Since alkyl chains from both sides doubly contribute to a single alkyl layer, an increment by a methylene group are (0.19/2) nm and (0.14/2) nm for normal and inclined alkyl chains, respectively.

The Gyroid phase consists of not flat but continuously curved layers (known as triply periodic minimal surface), resulting in continuous variation of molecular orientation. However, on the body-diagonals of unit cells, molecules must align along those because of the symmetry. Therefore, the same analysis as the orthogonal smectics applies. The previous paper [s12] studied the two Gyroid phases separated by the present chiral cubic phase in the phase diagram against the chain length (n). Their chain-length dependences of the cell constants are a / nm = 3.91 + 0.31n and a / nm = 4.72 + 0.22n for short- and long-chain members, respectively [s13]. Considering four molecules along the body-diagonal ($\sqrt{3}a$), we revealed the averaged molecular aggregation mode as the inclined chain state for short-chain members by 0.31 nm $(CH_2)^{-1} \times \sqrt{3}/4 \approx 0.134$ nm $(CH_2)^{-1}$. Since the experimental magnitude of 0.22 nm $(CH_2)^{-1} \times \sqrt{3}/4 \approx 0.095$ nm $(CH_2)^{-1}$ for the long-chain members just fits (0.19/2) nm $(CH_2)^{-1}$, we concluded that the chain is parallel to a body-diagonal with full interdigitation.

The molecules on the body diagonals of the present structural solution align parallel to those by symmetry. A body-diagonal contains four junctions with parallel molecules and vacant centers of two six-membered rings. Assuming that the parallel molecules are responsible for the chain-length dependence of the cell constant, a / nm = 6.91 + 0.38n [s13], we have 0.38 nm $(CH_2)^{-1} \times \sqrt{3}/4 \approx 0.165$ nm $(CH_2)^{-1}$, which is just the sum [(0.19/2) nm $(CH_2)^{-1}$ + (0.14/2) nm $(CH_2)^{-1}$]. Alkyl chains at two ends of a molecular core are in different environments; one between the three-way junctions and the other directed to the six-membered ring. They would differently contribute to the cell size. Considering their locations, we assign the straight conformation between the two junctions and the inclined one to the other.

References to Supporting Information

s1. Oka, T., *Acta Crystallogr. Sect. A*, **2022**, *78*, 430-436.
s2. Oka, T., *Acta Crystallogr. Sect. A*, **2023**, *79*. 51-58.
s3. Ozawa, K.; Yamamura, Y.; Yasuzuka, S.; Mori, H.; Kutsumizu, S.; Saito, K., *J. Phys. Chem. B*, **2008**, *112*, 12179-12181.
s4. Horiuchi, K.; Yamamura, Y.; Pelka, R.; Sumita, M.; Yasuzuka, S.; Massalska-Arodz, M.; Saito, K., *J. Phys. Chem. B*, **2010**, *114*, 4870-4875.
s5. Yamamura, Y.; Adachi, T.; Miyazawa, T.; Horiuchi, K.; Sumita, M.; Massalska-Arodz, M.; Urba, S.; Saito, K., *J. Phys. Chem. B*, **2012**, *116*, 9255-9260.
s6. Adachi, T.; Saitoh, H.; Yamamura, Y.; Hishida, M.; Ueda, M.; Ito, S.; Saito, K., *Bull. Chem. Soc. Jpn.*, **2013**, *86*, 1022-1027.
s7. Miyazawa, T.; Yamamura, Y.; Hishida, M.; Nagatomo, S.; Massalska-Arodz, M.; Saito, K., *J. Phys. Chem. B*, **2013**, *117*, 8293-8299.
s8. Saito, K.; Miyazawa, T.; Fujiwara, A.; Hishida, M.; Saitoh, H.; Massalska-Arodz, M.; Yamamura, Y., *J. Chem. Phys.*, **2013**, *139*, 114902.
s9. Yamamura, Y.; Tsuchiya, R.; Fujimura, S.; Hishida, M.; Saito, K., *J. Phys. Chem. B*, **2017**, *121*, 1438-1447.
s10. Yamamura, Y.; Murakoshi, T.; Iwagaki, S.; Osiecka, N.; Saitoh, H.; Hishida, M.; Galewski, Z.; Massalska-Arodz, M.; Saito, K., *Phys. Chem. Chem. Phys.*, **2017**, *19*, 19434-19441.
s11. Yamamura, Y.;, Murakoshi, T.; Hishida, M.; Saito, K., *Phys. Chem. Chem. Phys.*, **2017**, *19*, 25518- 25526.
s12. Yamamura, Y.; Nakazawa, Y.; Kutsumizu, S.; Saito, K., *Phys. Chem. Chem. Phys.*, **2019**, *21*, 23705-23712.
s13. Kutsumizu, S., Mori, H.; Fukatami, M.; Naito, S.; Sakajiri, K.; Saito, K., *Chem. Mater.*, **2008**, *20*, 3675-3687.